High stability SrTi$_{1-x}$Fe$_x$O$_{3-\delta}$ electrodes for oxygen reduction and oxygen evolution reactions†

Shan-Lin Zhang,[a,b] Dalton Cox,[a] Hao Yang,[b] Beom-Kyeong Park,[a] Cheng-Xin Li,[b] Chang-Jiu Li,[b] Scott A. Barnett [a,*]

[a.] Department of Materials Science and Engineering, Northwestern University, Evanston, Illinois 60208, USA. E-mail: s-barnett@northwestern.edu

[b.] State Key laboratory for Mechanical Behavior of Materials, School of Materials Science and Engineering, Xi'an Jiaotong University, Xi'an, Shaanxi, 710049, People's Republic of China. E-mail: licj@xjtu.edu.cn

Abstract

Sr(Ti$_{1-x}$Fe$_x$)O$_{3-\delta}$ (STF) has recently been explored as an oxygen electrode for solid oxide electrochemical cells (SOCs). Model thin film electrode studies show oxygen surface exchange rates that generally improve with increasing Fe content when x<0.5, and are comparable to the best Co-containing perovskite electrode materials. Recent results on porous electrodes with the specific composition Sr(Ti$_{0.3}$Fe$_{0.7}$)O$_{3-\delta}$ show excellent electrode performance and stability, but other compositions have not been tested. Here we report results for porous electrodes with a range of compositions from x = 0.5 to 0.9. The polarization resistance decreases with increasing Fe content up to x = 0.7, but increases for further increases in x. This results from the interaction of two effects - the oxygen solid state diffusion coefficient increases with increasing x, but the electrode surface area and surface oxygen exchange rate decrease due to increased sinterability and Sr surface segragation for the Fe-rich compositions. Symmetric cells showed no degradation during 1000 h life tests at 700 °C even at a current density of 1.5 A cm^{-2}, showing that all the STF electrode compositions worked stably in both fuel cell mode and electrolysis modes. The excellent stability may be explained by X-ray Photoelectron Spectroscopy (XPS) results showing that the amount of surface segregated Sr did not change during the long-term testing, and by relatively low polarization resistances that help avoid electrode delamination.

Introduction

Solid oxide cells (SOCs) have applications including fuel cells, electrolyzers, and reversible

cells for energy storage.[1–4] A major research focus for SOCs has been the development and testing of improved oxygen electrodes to provide improved cell performance and reduced operating temperature,[4–9] along with reduced problems with delamination during electrolysis operation.[10,11] However, as electrode materials have moved from strontium-doped lanthanum manganite (LSM) to more active mixed ionically and electronically-conducting (MIEC) materials such as $La_xSr_{1–x}Co_yFe_{1–y}O_{3–δ}$ (LSCF) and $Ba_{0.5}Sr_{0.5}Co_{0.8}Fe_{0.2}O_{3–δ}$ (BSCF),[12] more issues with cell stability have arisen. For example, LSCF electrode performance is observed to decrease with time due to Sr surface segregation[13–15]. For BSCF and related materials, Ba surface segregation and absorption of CO_2 typically cause rapid degradation during cell operation[16,17].

Aside from limited investigations of Ruddlesden-Popper phase materials with Ni as the B-site cation,[18] most of the MIEC electrodes considered have been perovskites utilizing Co and/or Fe as the main B-site cation. Recently, perovskites with Ti or Ca as one of the doping cations, such as $SrTi_{1–x}Fe_xO_{3–δ}$ (STF), have been explored as alternative SOC oxygen electrodes.[19,20] Tuller and co-workers carried out pioneering studies of the properties of various STF compositions in thin-film form[21–26]. The oxygen surface exchange coefficient values were found to be very competitive with the Fe/Co-based MIEC materials, although electrical conductivities are not as high. In a recent study of STF with x=0.7 as porous electrodes, low polarization resistance and high cell performance were demonstrated, and the good D* and k* values were verified.[27] It was also shown that the substitution of a small amount of Co for Fe in STF (x = 0.7) further improves properties and performance, and that the STF-based electrodes show very promising stability.[27] However, the porous-electrode studies have only been done for x = 0.7, so it is unknown how the Fe/Ti ratio affects performance and stability.

Here we report a comprehensive study of the electrochemical performance and stability of $SrTi_{1–x}Fe_xO_{3–δ}$ with x = 0.5 (STF-55), x = 0.6 (STF-46), x = 0.7 (STF-37), x = 0.8 (STF-28), and x = 0.9 (STF-19). Fundamental properties including phase structure, thermal expansion, electronic conductivity, oxygen non-stoichiometry, and oxygen transport coefficients are reported. Stability results from the symmetrical cells at different temperatures (650–750 °C) and different current densities (700 °C, 0.5–1.5 A cm^{-2}) show the excellent stability of the STF electrodes. Ni-based fuel electrode supported single cells with STF oxygen electrode yielded good performance both in SOFC and SOEC operating modes.

Results

Phase composition, conductivity, thermal expansion coefficient, and oxygen nonstoichiometry

The XRD patterns from $SrTi_{1-x}Fe_xO_{3-\delta}$ powders shown in Fig. 1(a) only have peaks representative of the cubic perovskite structure. The cubic lattice parameters (Fig. S1, (ESI†)) calculated from the XRD data decreased from 3.8869 ± 0.0014 Å to 3.86813 ± 0.0015 Å when the iron content increased from 0.5 to 0.9. The unit cell volume of STF decreases with increasing iron content, in agreement with the literature data.[28]

The total electrical conductivity of STF in air, presumably primarily electronic in nature, gradually increased with increasing iron content (Fig. 1 (b)). Increasing electronic conduction with increasing iron is probably associated with progressive delocalization of atomic levels and increasing bandwidth[29]. All compositions showed a similar temperature dependence, with maximum electrical conductivity values observed at $400 \sim 600$ °C ranging from 2.1 S cm^{-1} for x = 0.5 to 38 S cm^{-1} for x = 0.9. The maximum conductivity of 10 S cm^{-1} for x = 0.7 agrees reasonably well with prior reports.[27] Similarly, the maximum conductivity of 38 S cm^{-1} for x = 0.9 agrees well with prior data (35 S cm^{-1}).[30] Even though the conductivity of STF materials is lower than some of other perovskite oxygen electrode, such as LSM and LSCF, it should be sufficient for applications in thin (~15–20 μm) electrode functional layers and it may be more desirable to use higher-conductivity materials for the current collector layer.

Fig. 1 (c) shows relative elongation of STF, measured in air at 25–1000 °C. The elongation generally becomes more rapid with increasing temperature, in agreement with prior reports.[28] The average TEC (25–1000 °C) of STF increases with increasing x, from 12.3×10^{-6} K^{-1} for x = 0.5, to 17.2×10^{-6} K^{-1} for x = 0.7, to 27.1×10^{-6} K^{-1} for x = 0.9. The x = 0.7 value is consistent with a prior study[27]. The TEC value for x = 0.5 matches well with YSZ electrolytes (~11.5×10^{-6} K^{-1}), whereas for x = 0.7 the value is similar to that of the widely-used LSCF cathodes, while for x = 0.9 the values are quite high similar to those of high-performance MIEC cathodes such as SSC[31] and BSCF[32]. The increased TEC values are presumably due to higher oxygen loss and associated chemical expansion of the Fe-rich compositions at high temperature.

The thermogravimetric analysis (TGA) profile was recorded from 30 to 850 °C in air to evaluate the temperature dependent weight loss (Fig. S2 (ESI†)), which was directly related to the oxygen release properties. This measurement, combined with iodometric titration done at room

temperature prior to the TGA, was done to determine the non-stoichiometry (δ). As shown in Fig. 1(d), the δ value at room temperature increases with increasing x, from 0.08 for x=0.5, to 0.16 for x=0.7, to 0.24 for x=0.9. δ increases continuously with increasing temperature for the lower Fe content samples (x = 0.5–0.7), but for higher Fe content (x = 0.8, 0.9), δ remained approximately constant ~350 °C before increasing continuously up to 850 °C. Similar trends can be found in the SrFeO$_3$-based materials as reported in literature.[33] In general, δ at a given temperature is always higher for higher Fe content. For STF-37, the δ value at 700 °C is slightly higher than our previous study (0.249) which may be due to the different testing method. Also, the STF-19 sample shows a δ value of 0.36 at 800 °C, which is close to the δ value for SrFeO$_{3-\delta}$ (~0.37 at 800 °C) reported in literature.[34]
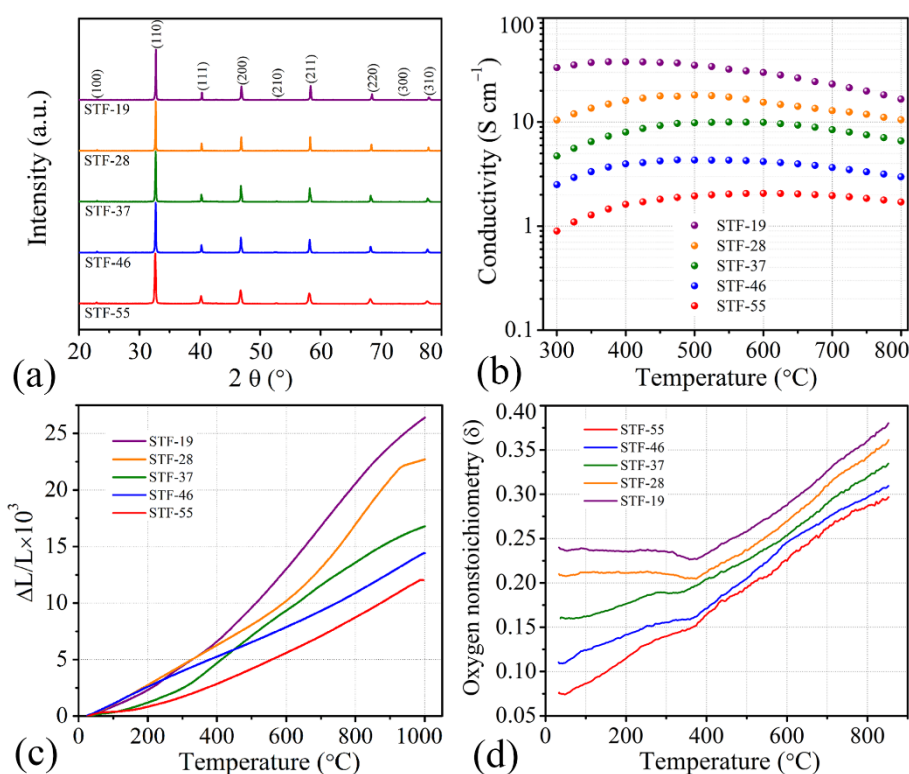

Fig. 1 Basic properties of STF: (a) XRD patterns, (b) total conductivity, (c) temperature dependence of relative elongation of STF in air, and (d) oxygen non-stoichiometry.

Microstructural analysis

Fracture cross-sectional SEM images of the as-prepared STF electrodes (Fig. S3 (ESI†)) show that thicknesses are ~15 μm and that the electrodes are bonded well with the GDC electrolyte. Figs. 2 (a) to (e) show polished cross-sectional images of portions of the STF electrodes with different x values. The structures are porous with well-connected electrode particles similar to those previously

reported for STF.[27] The size scale of the increases continuously with increasing x. Particle size distributions (Fig. S4 (ESI†)) obtained from a stereological analysis of the images in Fig. 2 shows this increase. The mean particle size (Fig. S4 (f) (ESI†)) increases with the increasing Fe content from 170 nm for x = 0.5 to 700 nm for x = 0.9. The mean particle size of ~340 nm for the STF-37 electrode agrees well with the value (~ 370 nm) previously obtained from 3D-tomographic measurements of similarly processed STF-37.[27]
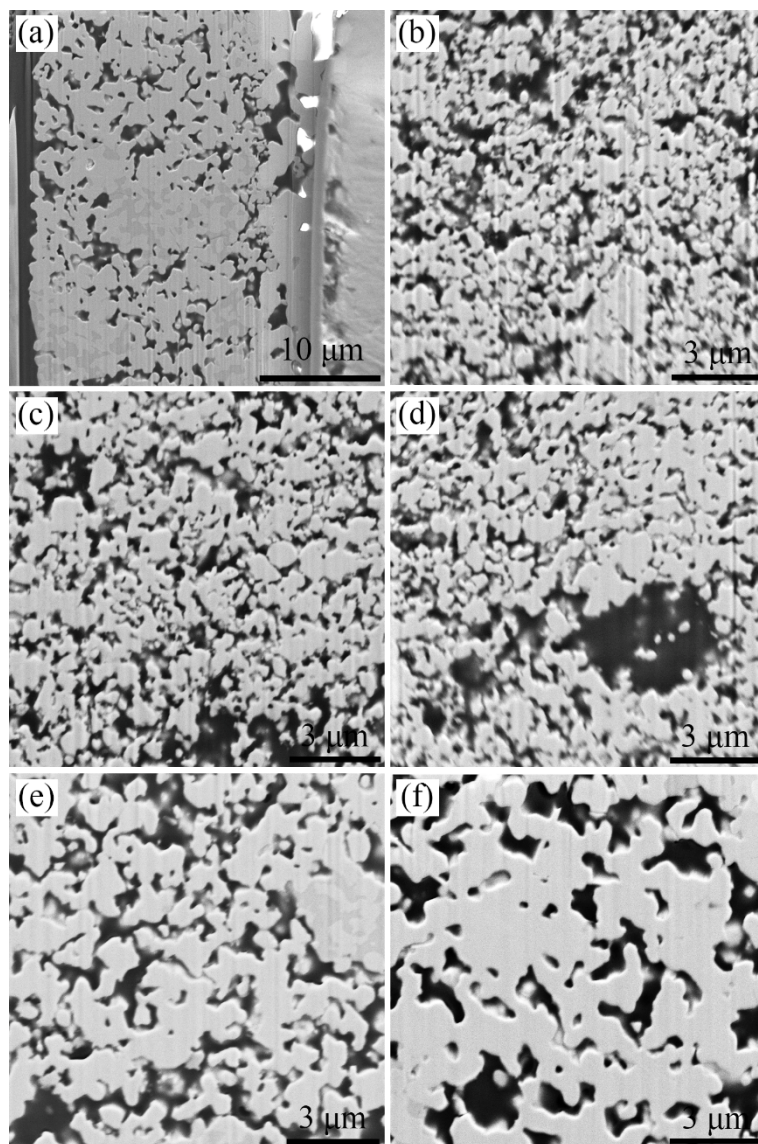

Fig. 2. Polished cross sectional images of electrodes; Low magnification image for (a) and high-magnifications for (b) STF-55, (c) STF-46, (d) STF-37, (e) STF-28, and (f) STF-19.

Fig. 3 shows the STF surface area (a) and porosity (b) *versus* x obtained from stereological analysis of the images in Fig. 2. The surface area values decrease with increasing x above 0.6, with an overall factor of 3 decrease from x = 0.5 to 0.9, matching the increases in particle size noted

above. The x = 0.5–0.8 electrodes have a similar porosity of 32%–37%, but for x = 0.9 the porosity

is decreased to 22%. These trends can be understood by noting the decreasing melting point with

increasing Fe content, *e.g.*, from 2080 °C for pure $SrTiO_3$[35] to 1340 °C for $SrFeO_3$.[36] Given that all

the electrodes were fired at the same temperature (1050 °C) and time (4 h), the increased electrode

feature sizes and decreased specific surface area with increasing x result from increased coarsening,

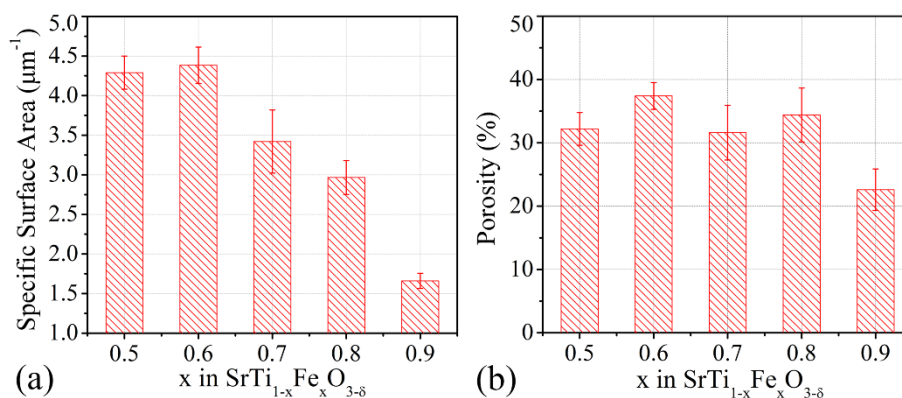while the decrease in porosity at high x indicate increased sintering.

Fig. 3. Electrode specific surface area (a) and porosity (b) from the 2D image analysis for different

STF electrodes.

Symmetric Cell Electrochemical Testing

Fig. 4 (a) shows typical Nyquist and Bode plots of EIS data for the STF electrode symmetric

cells, measured in air at 700 °C. The high-frequency real-axis intercepts of the impedance arcs are

all within a range (~0.6–0.75 Ω cm^2 at 700 °C) and were as expected for these electrolyte thickness

values. The high frequency intercepts were thus set to zero in the Nyquist plots in order to show

clearly the changes in the polarization responses. Increasing the iron content from x = 0.5 to x = 0.7

caused a substantial decrease in the overall polarization resistance; the Bode plot shows a broad

diffuse response at frequency ranging from ~ 1 to 1000 Hz, which diminishes with increasing x up

to 0.7. Further increases in x above 0.7 increased the electrode response, and the main peak narrowed

and shifted to ~ 10 Hz. The EIS data at other temperatures had a similar variation with iron content,

with the minimum total polarization resistance R_P at x = 0.7 (Fig. S5 (ESI†)), and the main responses

shifting to lower frequency with decreasing temperature.

Fig. 4 (a) also shows the EIS data obtained using an equivalent circuit consisting of an inductor

(L) primarily associated with measurement setup wires, the ohmic resistance (R1) associated with

the electrolyte, a modified Gerischer element (G) for the lower frequency response, and a R//QPE

element for the higher frequency response. The individual fitted responses are detailed in Fig. S6 (ESI†). Fig. 4 (b) gives a comparison of the total R_P versus inverse temperature for all the electrodes, obtained from the fitting data. The trends of R_P with x discussed above for 700 °C appear to be relevant at all temperatures, with R_P decreasing to a minimum value at x = 0.7, and then increasing with further increase in x. The R_P value for STF-37 at 700 °C (0.112 Ω cm^2) is very close to the data (0.117 Ω cm^2) reported in our previous study.[27] The activation energy (E_a) values calculated from linear fits to the ln(R_P) vs 1/T data in Fig. 3 (b), 1.043 ± 0.026 eV, showed no apparent variation with iron content and is close to the value reported previously for x = 0.7.[27]

The RQ-element resistance (R_Q) and Gerischer resistance (R_G) *versus* inverse temperature for all the electrodes obtained from the fits, are shown in Figs. 4 (c) and (d), respectively. The combination of G and RQ elements is commonly used for MIEC oxygen electrodes. The RQ element is usually associated with charge transfer between the electrode and electrolyte. The Gerischer element represents the impedance associated with the oxygen surface exchange and diffusion processes in the porous electrode, based on the Adler-Lane-Steele (ALS) model.[37–39] R_Q decreased for x increased from 0.5 to 0.7, but both remained approximately constant for further increases in x. R_G also decreased when the iron content increased from 0.5 to 0.7, but increased for x increased above 0.7. This variation, arising from a combination of variations in microstructure, oxygen transport coefficients, and Sr segregation with x, is discussed in section 4.1. The E_a values for R_Q and R_G were calculated from linear fits to the ln(R_Q) and ln(R_G) vs 1/T data and are shown in Fig. 4 (c) and (d), respectively. Increasing the iron content from x = 0.5 to x = 0.7 caused a substantial increase in the E_a values for R_Q from 0.386 to 0.649 eV. For further increases in x above 0.7, the E_a values for R_Q show little change. The E_a values for R_G, 1.305 ± 0.084 eV, showed no apparent variation with iron content. The relatively low E_a values for R_Q and high E_a values for R_G mean that R_G dominates at low temperatures, while R_Q becomes larger at high temperatures. The apparent activation energy for R_P, shown in Fig. 4 (b), falls between that of R_Q and R_G, as expected.
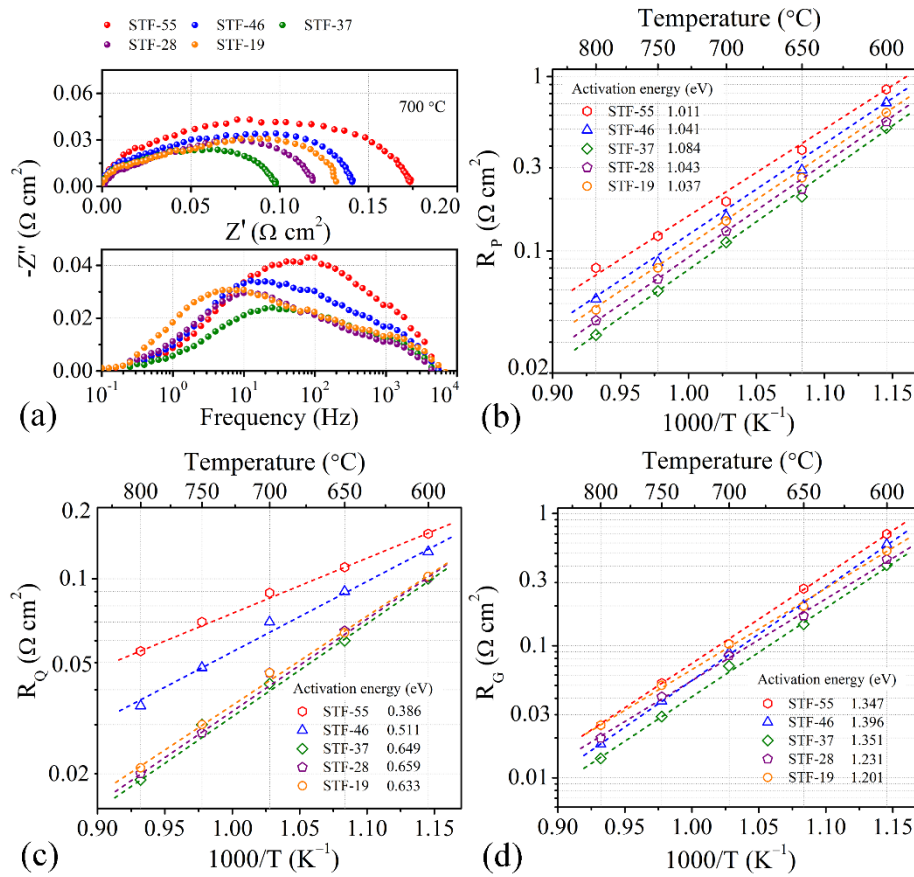
Fig. 4 (a) Typical Nyquist and Bode plots of EIS data measured at 700 °C. All the data were the steady state values obtained after the annealing at 850 °C for 20 hours. The high frequency intercepts in the data were set to zero, in order to facilitate comparison of the polarization arcs; Arrhenius plots of the total electrode polarization resistance values (b), R_Q values (c), and R_G values (d) measured from the EIS fitting results.

Symmetrical cell life tests

In order to investigate the stability of STF electrodes, ~ 1000 h life tests on STF-electrode symmetric cells were carried out at 700 C. Fig. 5 shows representative Nyquist and Bode plots of the EIS data taken periodically during the test for STF-37 electrode cells without and with current in (a) and (b) respectively. For both tests, the response changes significantly in the first ~ 200 hours – the main response at ~ 10 Hz (associated to R_G) decreases significantly and shifts to higher frequency (~ 100 Hz), while the higher frequency response (R_Q) decreases slightly. The resulting decreases in R_P were substantial. After ~ 200 h of testing, however, the EIS spectra and R_P values become mostly stable.
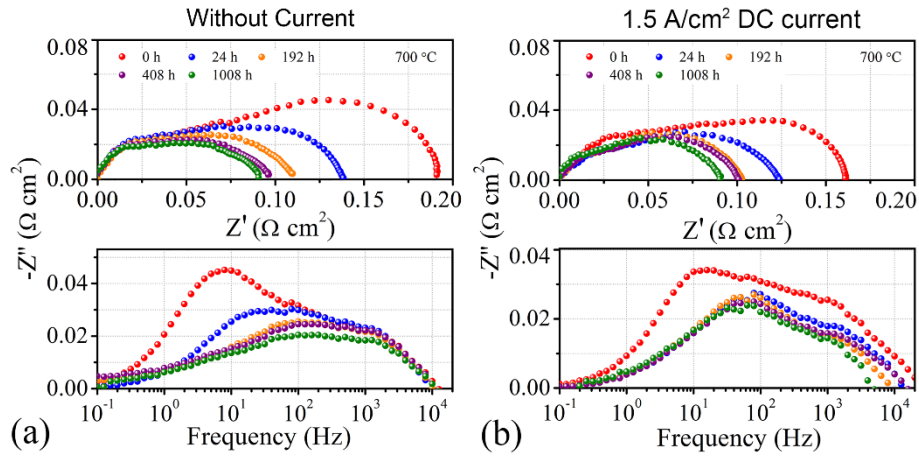
Fig. 5 Evolution of Typical Nyquist and Bode plots of EIS data measured at 700 °C for the symmetric cells with STF-37 electrode. (a) Without current; (b) With 1.5 A cm^{-2} DC current.

Fig. 6 plots R_P versus time, taken from the intercepts of life-test EIS data such as that shown in Fig. 5. Figs. 6 (a) to (c) shows the evolution of R_P with time for cells under different temperatures without current. Figs 6 (d) to (f) shows R_P versus time for cells tested at 700 °C at different current densities. In all cases, there was an initial break-in period during which R_P decreased, after which R_P remained stable within measurement accuracy. A similar initial R_P decrease was observed previously for STF-based electrodes [27] and is probably an electrode thermal or current activation as has been widely observed for other electrodes, *e.g.,* LSM–YSZ[40] and Pr$_2$NiO$_{4+\delta}$-based electrodes[18]. The time to reach steady state decreased significantly with increasing temperature (Figs. 6 (a)-(c)), from ~ 600 h at 650 °C to ~ 100 h at 750 °C. On the other hand, R_P stabilized more rapidly in tests with current (Figs. 6 (d)-(f)), but the final stable R_P values were the same regardless of the current density. The cell ohmic resistance (Fig. S7 (ESI†)) also showed a short initial break-in period (~ 50 h) before becoming reasonably stable, and the final resistance values were similar with and without current.
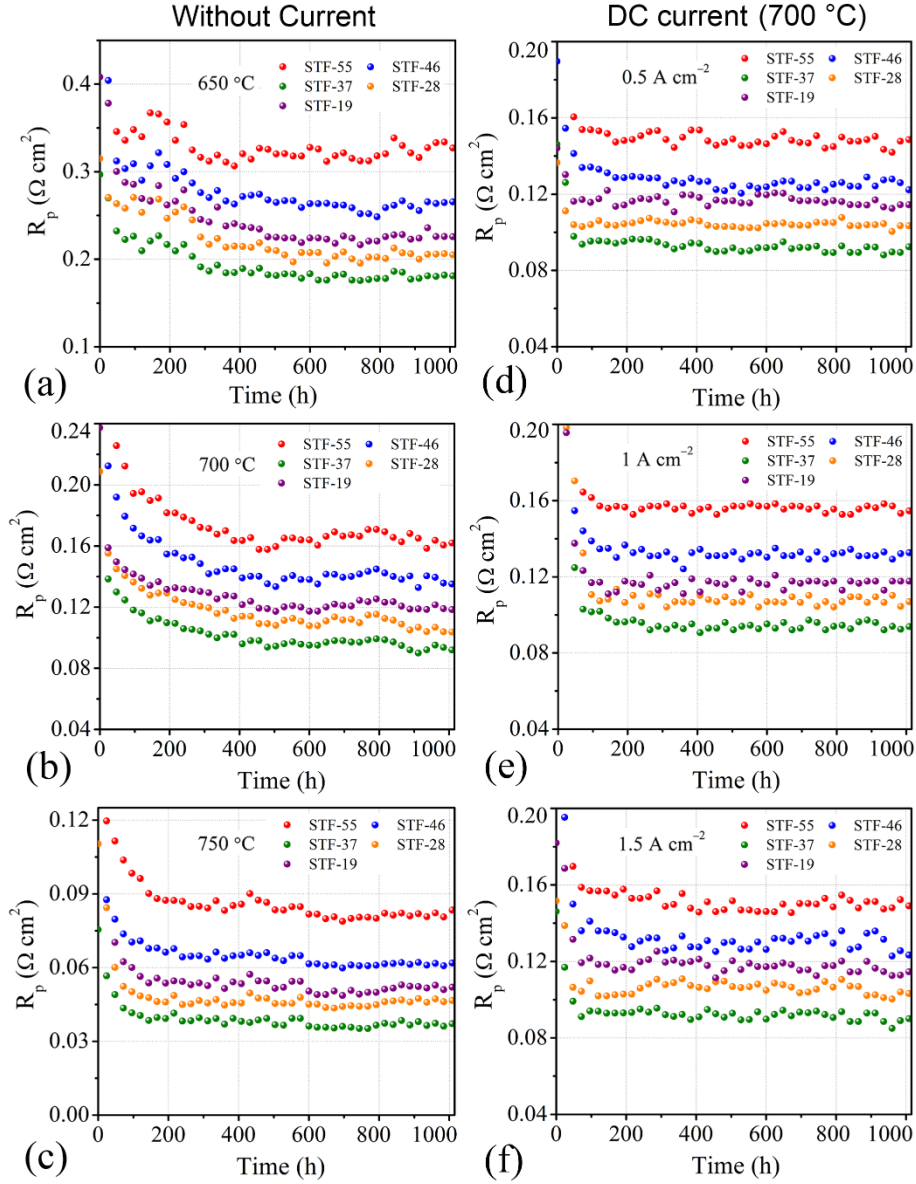
Fig. 6 Evolution of cell polarization resistance (R_P) at 700 °C for the symmetric cells with STF electrodes; (a), (b), and (c) at different temperatures without current: (a) 650 °C, (b) 700 °C, (c) 750 °C; (e), (d), and (f) tested under 700 °C at different current densities: (e) 0.5 A cm^{-2}, (d) 1.0 A cm^{-2}, and (f) 1.5 A cm^{-2}.

The electrodes were observed in fracture cross sectional SEM images after the various life tests, but there were no signs of microstructure change or delamination in any case – see Fig. S8, S9 and S10 (ESI†) compared with the as-prepared electrodes in Fig. S3 (ESI†).

The surface compositions of STF electrodes were tested in the as-prepared state and after aging in air at 700 °C for 1000 h using X-ray Photoelectron Spectroscopy (XPS). Typical survey Sr 3d spectra for as-prepared and aged STF-55 electrodes are shown in Fig. 7 (a) and (c), respectively. It

can be seen that Sr has three binding-energy states, corresponding to Sr in STF (Sr–O 1), SrO (Sr–O 2), and $SrCO_3$.[26] The latter presumably arises from sample exposure to CO_2 (in air) during cell aging or transfer from the furnace to the XPS, and can be attributed to the reaction with segregated SrO.[41] Thus, the higher $SrCO_3$ peak intensity and lower Sr-O peak intensity after aging indicates more SrO on the surface reacted with CO_2 during the aging. The Sr peak intensity relative to the sum of the other cation peaks is plotted versus Fe content in Fig. 7 (b) and (d) for the as-prepared and aged samples, respectively. There is a clear increase in the relative Sr intensity with increasing Fe content from ~1.5 for STF-55 to ~ 2.4 for STF-19. The observation of Sr segregation on STF agrees with prior results on thin-film[41] and porous STF samples measured by XPS,[27] where the surface Sr/(Ti + Fe) ratio was ~1.7 for STF-37. More important, the Sr/(Ti + Fe) ratio for the aged samples is nearly unchanged, indicating that the Sr segregation does not increase during ageing.
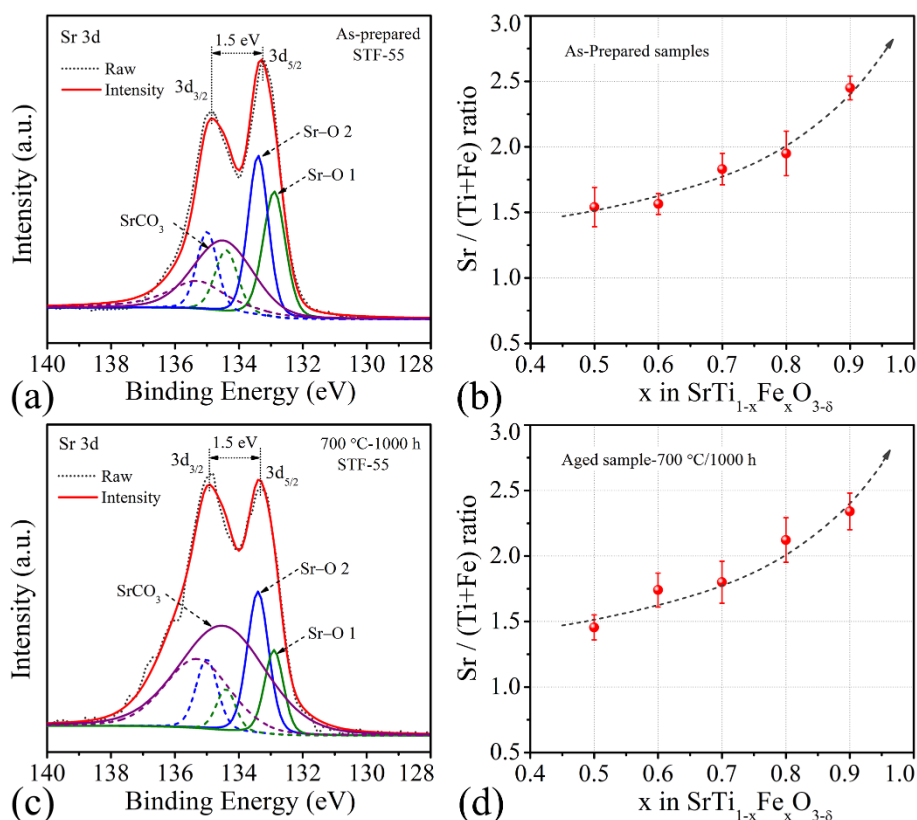

Fig. 7 XPS Sr 3d spectra from as-prepared (a) and 1000 h aged (c) STF-55 electrodes; Ratio of A- and B-site cations on electrodes surface as a function of Fe content, measured by XPS, for as-prepared (b) and 1000 h aged (d) samples.

Performance of full cells with STF-37 and LSCF/GDC electrode

The STF oxygen electrodes were tested in full cells to evaluate their performance under

practical cell operating conditions. Similar cells with the commonly-used LSCF/GDC oxygen electrodes were also tested in the same condition for comparison. Fig. S11, (ESI†) shows cross-sectional SEM views of the cells. Fig. 8 (a) and (b) show typical electrochemical characteristics under representative fuel cell conditions, i.e., in air and 3% H_2O + 97% H_2 fuel. Peak power densities for STF-37 cell ranged from 1.92 W cm^{-2} at 800 °C to 0.42 W cm^{-2} at 600 °C. These values are slightly higher than those of the LSCF/GDC cell. Figs. 8 (c) and (d) show the voltage versus current density at different temperatures in electrolysis mode; the conditions are the same as in Fig. 8 (a) and (b), except that the fuel composition is 50% H_2O + 50% H_2. In this operating mode, the STF electrode cell yielded 25~30 % higher current density (e.g., 2.33 A cm^{-2} at 800 °C) at a typical electrolysis voltage of 1.3 V compared to LSCF-GDC (1.68 A cm^{-2} at 800 °C).

In Figs. 8 (c) and (d), the j–V curves show more curvature for LSCF/GDC cell than for STF-37 cell, especially at higher temperatures. The EIS data for the full cells measured in 50% H_2O + 50% H_2 (Fig. S12, (ESI†)) at 700 °C (OCV condition) indicates the ohmic resistance and polarization resistance from fuel electrode, oxygen electrode, and gas diffusion are very close for the two types cells. Therefore, the lower electrolysis performance of LSCF/GDC cell can be attributed to the non-linear dependence of j–V curves, not the gas concentration polarization from Ni–YSZ fuel electrodes. However, future research is needed to understand why the j–V curves are bending.
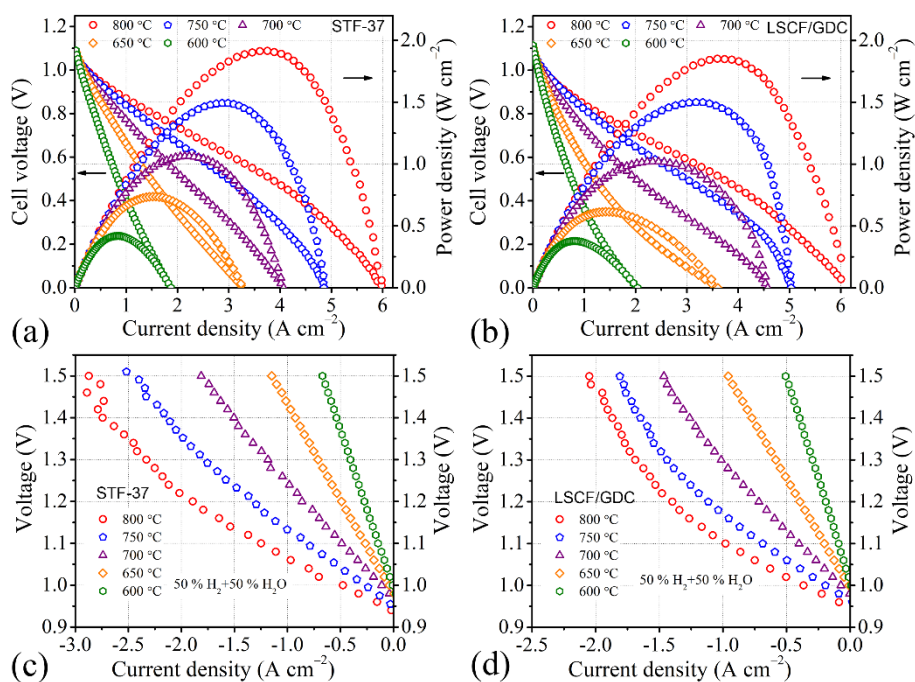
Fig. 8 Voltage and power density versus current density for a full cell with STF-37 (a) and LSCF/GDC (b) electrode measured at different temperatures in air and 3% H_2O humidified hydrogen. Voltage versus current density for a full cell with STF-37 (c) and LSCF/GDC d) electrode measured at different temperatures in air and 50 vol% H_2 + 50 vol% H_2O.

Discussion

Electrode performance

The EIS data (Fig. 4) show that x = 0.7 yields the lowest total electrode resistance R_P. Figure 9 shows the breakdown of R_P into its two main components: R_G shows a clear minimum at x = 0.7, while R_Q decreases with increasing x up to 0.7 and remains constant at higher x. The decreased R_Q value may have resulted from increased electrode/electrolyte contact area, due to the higher sinterability of the Fe-rich compositions noted in section 3.2. Note that a high-frequency response associated with charge transfer between the electrode and electrolyte is also observed in MIEC thin-film electrodes;[42, 43] however, the resistance should be enhanced in the present porous electrodes because they have a much smaller electrode-electrolyte contact area than thin films. The minimum in R_G at x = 0.7 shown in Fig. 9 is different than the thin-film STF results, where the surface resistance decreases continuously with increasing x.[21] However, R_G for a porous electrode is not directly comparable to thin-film surface resistance for two reasons. First, R_G depends not only on surface resistance, as in thin films, but also on oxygen diffusivity. Second, R_G depends strongly on electrode microstructure, different than the simple planar thin film. Thus, the changes in microstructure with x shown in Fig. 2 are expected to impact R_G, In particular, the decrease in surface area with increasing x should tend to increase the resistance.
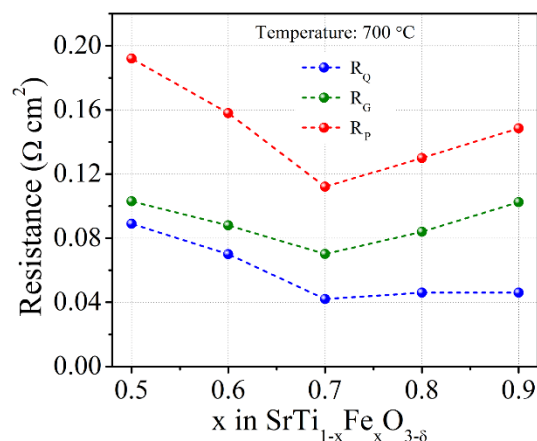

Fig. 9. G and R_Q values for different STF at 700 °C from the EIS fitting shown in Fig. S6.

Adler–Lane–Steele model analysis is carried out here to account for these effects and thereby obtain the oxygen solid state diffusion coefficient D* and the oxygen surface exchange coefficient k*. The analysis follows that described in Ref,[44,45] and is also described in the supplement. The Gerischer resistance R_G and time constant t_G values from the EIS fitted Gerischer response (Table S1 and Table S2, (ESI†)) are used along with the oxygen non-stoichiometry (Table S3 (ESI†)), electrode porosity (Fig. 3 (b)), surface area (Fig. 3 (a)), and solid-phase tortuosity (given in Table S4, (ESI†)). The other parameters needed include the oxygen vacancy concentration and thermodynamic factor; for this, values from our previous study for STF-37 were used, and they were assume to not vary with the Fe/Ti ratio.[27]

The resulting D* and k* values are shown in Fig. 10. Values for both D* and k* for STF-37 samples are close to our previous study. [27] D* increases continuously with increasing Fe content, with the biggest increase between x = 0.5 and 0.6. At 700 °C, for example, the D* value is 5 times higher for STF-19 compared to STF-55. k* decreases slightly with increasing x from 0.5–0.7. Thus, the slight decrease in R_G from x = 0.5–0.7 (Fig. 9) is mainly due to the increase in D*, mitigated by slight decreases in k* and surface area. On the other hand, from x = 0.7–0.9, the decreases in k* and surface area become more dominant compared to the increase in D*, resulting in the increase in R_G in Fig. 9.

The results in Figure 10 are the first indication of how D* varies with Fe content in STF, since the prior thin-film studies did not yield D* values. The increase in D* with increasing Fe content can be explained by the increase in oxygen vacancy concentration implied by the increased oxygen non-stoichiometry (Fig. 1(d)). The magnitude of the k* values In Fig. 10 agree very well with those reported for STF thin films with x = 0.5 – 0.8 at 650 °C (6–7 $\times 10^{-7}$ cm s^{-1}).[25] However, the decrease in k* with increasing x shown in Fig. 10 is the opposite of the trend reported previously for thin films,[21,25,46] although in all cases the variations with x are weak. The decrease of k* with increasing x may be related to the increasing Sr surface segregation as shown in Fig. 7.
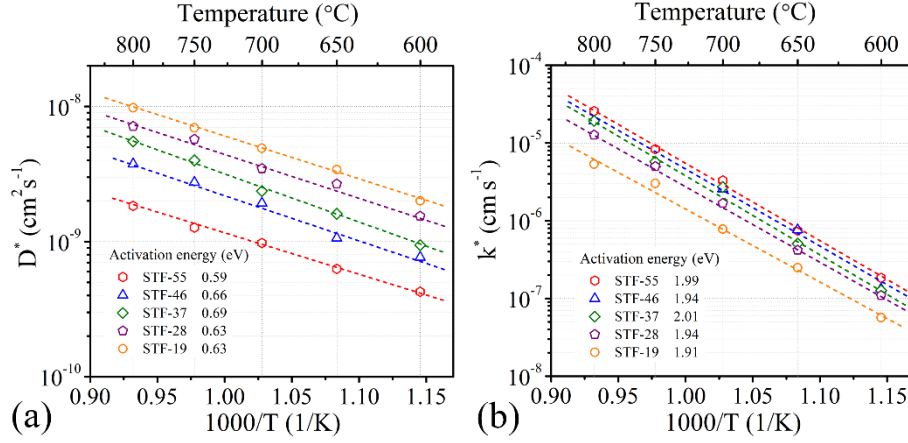
Fig. 10 (a) D* and (b) k* versus temperature for STF materials.

The lowest polarization resistance in the present study is for the STF-37 electrode, with ~0.1 $\Omega\,cm^2$ at 700 °C. This is lower than typical values for the widely used LSCF electrode.[27] The present full cells with STF-37 electrodes yield excellent performance at ≥ 700 °C, with similar fuel-cell power densities as cells with LSCF/GDC composite electrode, and higher current densities than the LSCF/GDC cell in electrolysis mode. At temperature < 700 °C, cell performance is worse, in part of the increased STF R_P value but also because the present full cells are not optimized for low-temperature operation. For use in low-temperature SOCs, e.g., utilizing an $La_{0.8}Sr_{0.2}Ga_{0.8}Mg_{0.2}O_{3-\delta}$ (LSGM) electrolyte instead of YSZ,[47] STF performance needs to be improved. As reported in our previous study, small amounts of Co doping on the Fe site can improve the conductivity and oxygen transport coefficient, thus reducing R_P to 0.2 $\Omega\,cm^2$ at 600 °C.[27] It was found that Co doping increases both D* and k* and decreases Sr surface segregation – the same correlation between k* and Sr segregation seen in the present results. Finally, according to the ALS model, increasing the electrode surface area, *i.e.,* by decreasing STF particle sizes, is another possible method to reduce R_P.

Electrode stability

The symmetric cell life tests show excellent stability of the STF electrodes, much better than the widely-used LSCF electrodes, where the degradation is mainly caused by the increasing amount of Sr segregation during cell operation.[15,48] Although a relatively large amount of segregated Sr is present on STF electrode surfaces, the amount of segregated Sr does not increase during life tests, possibly explaining the good stability. Also, SEM images (Figs. S9 and S10, (ESI†)) show smooth particle surfaces before and after life tests, indicating that the segregated Sr does not aggregate into

particles over time. This is different than LSCF, where Sr-based particles are observed to form on LSCF surfaces during high-temperature ageing.[49] Thus, the good stability of the STF electrodes may be explained, at least in part, by the stable amount and morphology of segregated Sr.   The reason for the stable STF surface is not known, and detailed surface science studies will likely be required to answer this.

The symmetric cells also showed excellent stability in tests carried out with current densities up to 1.5 A cm^{-2} (Fig. 5). This is notable given that LSM–YSZ oxygen electrodes degrade under electrolysis operation at such high current density values.[50,51] (Note that in these symmetric cells, one electrode operates in electrolysis mode and the other operates in fuel cell mode.) It was also shown that the overpotential could be estimated from the R_P value and the current density using a simplified symmetric form of the Butler-Volmer equation. Table 1 gives the overpotential values estimated in this way for the present electrodes at 1.5 A cm^{-2}. The present STF electrodes have R_p values low enough at 700 °C to maintain overpotential $\ll$ 0.2 V, explaining the absence of any fracture.

Table 1 Overpotential for STF electrodes tested under 1.5 A cm^{-2} at 700 °C

Electrodes	STF-55	STF-46	STF-37	STF-28	STF-19
EA (V)	0.146	0.132	0.105	0.12	0.126

Summary & Conclusions

A comprehensive study of $Sr(Ti_{1-x}Fe_x)O_{3-\delta}$ (x = 0.5 – 0.9) oxygen electrodes is presented. The results show that the Fe content has significant influence on the microstructure, basic properties, and electrochemical performance of STF electrodes. With increasing iron content, STF exhibits higher electronic conductivity, oxygen ionic conductivity[28], and oxygen bulk diffusion coefficient. However, these factors are mitigated by decreasing oxygen surface exchange coefficient – possibly related to increased Sr segregation – and decreased electrode surface area – due to increased coarsening and sintering of the lower melting point Fe-rich compositions. The interface resistance between STF and the GDC electrolyte decreased with increasing Fe content up to x = 0.7, probably due to improved interfacial contact between GDC and the more-sinterable Fe-rich STF.   These factors combine to give the 70% Fe content STF (STF-37) the lowest polarization resistance of the compositions studied. All of the compositions yielded stable operation, probably due at least in part

to the stable amount of segregated Sr during cell operation. The optimal STF-37 electrode yields low polarization resistance and excellent stability at 700 °C in both SOFC and SOEC operation with current density as high as 1.5 A cm^{-2}, characteristics that make it competitive or better than other MIEC electrodes such as LSCF.

Experimental

Materials synthesis and cell fabrication

Powders with compositions SrTi$_{1-x}$Fe$_x$O$_{3-\delta}$ with x = 0.5 (STF-55), x = 0.6 (STF-46), x = 0.7 (STF-37), x = 0.8 (STF-28), and x = 0.9 (STF-19) were synthesized by solid state reaction. SrCO$_3$ (Sigma-Aldrich, 99.9%), TiO$_2$ (Alfa Aesar, 99.9%), and Fe$_2$O$_3$ (Alfa Aesar, 99.8%), were the starting materials. Stoichiometric amounts of the powders were ball milled in ethanol for 24 hours with zirconia balls as milling medium. The mixed powders were then dried and calcined at 1100 °C for 10 hours. The resulting STF powders were subsequently ball milled in ethanol for another 48 hours as described above and dried. The symmetrical cells had Gd$_{0.1}$Ce$_{0.9}$O$_{2-\delta}$ (GDC) electrolytes. The sintered GDC pellets (1450 °C/5 h) had a diameter of 16 mm and a thickness of ~0.5–0.6 mm. STF inks were prepared by mixing STF powders and binder (V-737, Heraeus) with weight ratio of 1 : 1.2 in a three-roll mill. The inks were then screen printed on both sides of the electrolyte pellet followed by firing at 1050 °C for 4 h. The electrode thickness was 15–20 μm and the electrode area was 0.5 cm^2.

Ni–Y$_{0.16}$Zr$_{0.92}$O$_{2-\delta}$ (Ni–YSZ) supported half cells were prepared by tape casting with 45 wt.% NiO + 45 wt.% YSZ + 10 wt.% starch (pore former) as the support layer, 50 wt.% NiO + 50 wt.% YSZ as the fuel electrode, and YSZ as the electrolyte. In order to reduce the firing temperature, 3% mol Fe$_2$O$_3$ was added in the electrolyte as the sintering aid. Then the cells were co-fired at 1250 °C for 2 h. Next, in order to prevent any reactions between YSZ electrolyte and STF electrodes, a GDC interlayer was screen printed on the YSZ electrolyte and then fired at 1200 °C for 2 h. The STF oxygen electrodes were screen printed onto the GDC interlayer and calcined at 1050 °C for 4 h. In order to compare the performance of STF with LSCF-based electrodes, identical full cells were prepared but with LSCF-GDC (50 wt.% : 50 wt.%) electrodes. Commercial LSCF powder (Praxair) and GDC powder (Fuel Cell Material) were used to make the ink as described above and the screen-printed electrodes were fired at 1100 °C for 2 h. The total effective area of the oxygen electrode is 0.5 cm^2.

Materials characterization

The phase structures of the STF powders were characterized *via* X-ray diffraction (XRD) analysis (Xpert PRO, PANalytical, Netherlands). Dense bar-shaped pellets with dimensions of ~5 mm × 5 mm × 25 mm, prepared by sintering at 1300 °C for 5 h, were used for conductivity and thermal expansion coefficient (TEC) measurements. The electrical conductivity was measured via a four-probe DC method with a Keithley 2400 source meter. The TEC was measured by a solid linear expansion coefficient apparatus (DIL 402C, NETZSCH). The oxygen non-stoichiometries (δ) of the STF powders at room temperature and elevated temperatures were investigated by iodometric titration and thermogravimetric analysis (TGA), respectively. The TGA was performed on a thermoanalyzer (NETZSCH model STA 449C) between 30 and 850 °C with a heating rate of 10 °C min^{-1} in air. The iodometric titration procedure and calculation of δ can be found elsewhere[33, 52]. The surface composition of the electrodes was analyzed using X-ray Photoelectron Spectroscopy (XPS, Thermo Fisher ESCALAB Xi+). Cell microstructures were examined via scanning electron microscopy SEM (Hitachi SU8030 and TESCAN MIRA 3 LMH). The porosity and specific surface area of the electrodes were examined by the 2D microstructure images from the FIB-SEM (FEI Helios) analysis. The tortuosity factor was estimated by an overlapping spheres model for high solids volume fraction.[53]

Electrochemical measurements

For symmetric cells, gold contact grids (Heraeus Inc., Pennsylvania) were screen printed on both sides to facilitate current collection. The EIS measurements were conducted at 600–800 °C using an IM6 Electrochemical Workstation (ZAHNER, Germany) with a 20 mV AC signal in the frequency range of from 0.1 Hz to 100 kHz. Prior to testing, the cells were annealed at 850 °C for 20 hours. The EIS tests were then performed starting at 800 °C and then reducing the temperature, with the final test at 600 °C. The symmetric cells were life tested for > 1000 h at 650, 700, and 750 °C with both electrodes exposed to ambient air without current. Other three cells were tested with a constant direct current of 0.5, 1, and 1.5 A cm^{-2} (Keithley 2420 power supply) at 700 °C. The similar configuration of the test can be found in our previous study[27]. In this condition, the electrode on one side was working under SOFC mode and the other side was working under SOEC mode. EIS measurements were made once per day during the life tests with no applied DC potential.

For the full cell testing, a silver grid (Heraeus Inc., Pennsylvania) was screen printed onto the

oxygen electrode to enhance current collection. The cells were sealed onto alumina tubes with silver paste (DAD-87, Shanghai Research Institute of Synthetic Resins). For fuel cell testing, 100 sccm humidified H_2 (97% H_2 + 3% H_2O) was supplied to the Ni–YSZ anode while 150 sccm air was supplied to the STF or LSCF-GDC cathode, in the temperature range of 600–800 °C. For electrolysis testing, the oxygen electrode was exposed to air (150 sccm) while 100 sccm H_2 flowed through a heated H_2O-containing bubbler was supplied to the Ni–YSZ fuel electrode. In this study, the water in the bubbler was maintained at 81.7 °C, entraining 50 vol% water in the H_2 flow. Current–voltage curves were measured at 10 mV increments over the relevant voltage ranges for fuel cell and electrolysis operation.

Conflicts of interest

The authors declare no competing interests.

Acknowledgements

References

1. B. C. H. Steele and A. Heinzel, *Nature*, 2001, **414**, 345–352.

2. E. D. Wachsman, C. A. Marlowe and K. T. Lee, *Energy Environ. Sci.*, 2012, **5**, 5498–5509.

3. D. M. Bierschenk, J. R. Wilson and S. A. Barnett, *Energy Environ. Sci.*, 2011, **4**, 944–951.

4. C. Graves, S. D. Ebbesen, S. H. Jensen, S. B. Simonsen and M. B. Mogensen, *Nature Mater.*, 2014,

14, 239–244.

5. C. Duan, D. Hook, Y. Chen, J. Tong and R. O'Hayre, *Energy Environ. Sci.*, 2017, **10**, 176–182.

6. A. Jun, J. Kim, J. Shin and G. Kim, *ChemElectroChem*, 2016, **3**, 511–530.

7. Y. Chen, W. Zhou, D. Ding, M. Liu, F. Ciucci, M. Tade and Z. Shao, *Advan. Energy Mater.*, 2015, **5**, 1500537–1500571

8. Z. Gao, L. V. Mogni, E. C. Miller, J. G. Railsback and S. A. Barnett, *Energy Environ. Sci.*, 2016, **9**, 1602–1644.

9. J. D. Baek, Y.-J. Yoon, W. Lee and P.-C. Su, *Energy Environ. Sci.*, 2015, **8**, 3374–3380.

10. M. S. Khan, X. Xu, J. Zhao, R. Knibbe and Z. Zhu, *J. Power Sources*, 2017, **359**, 104–110.

11. K. Chen, N. Ai and S. P. Jiang, *Int. J. Hydrogen Energy*, 2012, **37**, 10517–10525.

12. Z. Shao and S. M. Haile, *Nature*, 2004, **431**, 170–173.

13. Y. Liu, K. Chen, L. Zhao, B. Chi, J. Pu, S. P. Jiang and L. Jian, *Int. J. Hydrogen Energy*, 2014, **39**, 15868–15876.

14. L. Zhao, J. Drennan, C. Kong, S. Amarasinghe and S. P. Jiang, *J. Mater. Chem. A*, 2014, **2**, 11114–11123.

15. H. Wang and S. A. Barnett, *ECS Transactions*, 2017, **78**, 905–913.

16. D. Garcés, H. Wang, S. A. Barnett, A. G. Leyva and L. V. Mognid, *ECS Transactions*, 2017, **78**, 1011–1020.

17. Y. Liu, X. Zhu and W. Yang, *AIChE Journal*, 2015, **61**, 3879–3888.

18. J. G. Railsback, Z. Gao and S. A. Barnett, *Solid State Ionics*, 2015, **274**, 134–139.

19. S. Molin, W. Lewandowska-Iwaniak, B. Kusz, M. Gazda and P. Jasinski, *J. Electroceram.*, 2012, **28**, 80–87.

20. C. Lim, S. Sengodan, D. Jeong, J. Shin and G. Kim, *Int. J. Hydrogen Energy*, 2019, 44. 1088–1095.

21. W. Jung and H. L. Tuller, *Solid State Ionics*, 2009, **180**, 843–847.

22. A. Rothschild, W. Menesklou, H. L. Tuller and E. Ivers-Tiffée, *Chem. Mater.*, 2006, **18**, 3651–3659.

23. M. Kuhn, J. J. Kim, S. R. Bishop and H. L. Tuller, *Chem. Mater.*, 2013, **25**, 2970–2975.

24. W. Jung and H. L. Tuller, *J. Electrochem. Soc.*, 2008, **155**, B1194–B1201.

25. W. Jung and H. L. Tuller, *Adv. Energy Mater.*, 2011, **1**, 1184–1191.

26. Y. Chen, W. Jung, Z. Cai, J. J. Kim, H. L. Tuller and B. Yildiz, *Energy Environ. Sci.*, 2012, **5**, 7979.

27. S.-L. Zhang, H. Wang, M. Y. Lu, A.-P. Zhang, L. V. Mogni, Q. Liu, C.-X. Li, C.-J. Li and S. A.

Barnett, *Energy Environ. Sci.*, 2018, **11**, 1870–1879.

28. V. V. Kharton, A. V. Kovalevsky, A. P. Viskup, J. R. Jurado, F. M. Figueiredo, E. N. Naumovich and J. R. Frade, *J. Solid State Chem.*, 2001, **156**, 437–444.

29. A. Rothschild, W. Menesklou, H. L. Tuller and E. Ivers-Tiffée, *Chem. Mater.*, 2006, **18**, 3651–3659.

30. G. Yang, W. Zhou, M. Liu and Z. Shao, *ACS App. Mater. Inter.*, 2016, **8**, 35308–35314.

31. S. Yang, T. He and Q. He, *J. Alloy. Compd.*, 2008, **450**, 400–404.

32. R. Kriegel, R. Kircheisen and J. Töpfer, *Solid State Ionics*, 2010, **181**, 64–70.

33. G. Lei, L. Qiang, S. Liping, X. Tian, H. Lihua, Z. Hui and G. Jean-Claude, *J. Mater. Chem. A*, 2018, **6**, 15221–15229.

34. J. Yoo, C.-Y. Yoo, J.-H. Yu and A. J. Jacobson, *J. Am. Ceram. Soc.*, 2017, **100**, 2690–2699.

35. O. Madelung, U. Rössler and M. Schulz, Ternary Compounds, Organic Semiconductors. Landolt-Börnstein - Group III Condensed Matter (Numerical Data and Functional Relationships in Science and Technology), *Springer Berlin Heidelberg, Berlin, Heidelberg,*, 2000, **41**, DOI: 10.1007/10717201_531.

36. E. Ksepko, *Int. J. Hydrogen Energy*, 2018, **43**, 9622–9634.

37. Y. Lu, C. Kreller and S. B. Adler, *J. Electrochem. Society*, 2009, **156**, B513.

38. K. Yakal-Kremski, L. V. Mogni, A. Montenegro-Hernández, A. Caneiro and S. A. Barnett, *J. Electrochem. Soc.*, 2014, **161**, F1366–F1374.

39. J. Railsback, G. Hughes, L. Mogni, A. Montenegro-Hernández and S. Barnett, *J. Electrochem. Soc.*, 2016, **163**, F1433–F1439.

40. G. Hughes, K. Yakal-Kremski, A. Call and S. Barnett, *Electrochem. Soc.*, 2012, **159**, F858–F863.

41. W. Jung and H. L. Tuller, *Energy Environm. Sci.*, 2012, **5**, 5370–5378.

42. Y. Li, L. M. Wong, C.-C. Yu, S. Wang and P.-C. Su, *Surf. Coat. Tech.*, 2017, **320**, 344–348.

43. D. Chen, C. Chen, Y. Gao, Z. Zhang, Z. Shao and F. Ciucci, *J. Power Sources*, 2015, **295**, 117–124.

44. K. Yakal-Kremski, L. V. Mogni, A. Montenegro-Hernández, A. Caneiro and S. A. Barnett, *J. Electrochem. Soc.*, 2014, **161**, F1366–F1374.

45. A. Flura, C. Nicollet, V. Vibhu, B. Zeimetz, A. Rougier, J.-M. Bassat and J.-C. Grenier, *J. Electrochem. Soc.*, 2016, **163**, F523–F532.

46. C.-Y. Yoo and H. J. M. Bouwmeester, *Phy. Chem. Chem. Phy.*, 2012, **14**, 11759–11765.

47. Z. Gao, H. Wang, E. Miller, Q. Liu, D. Senn and S. Barnett, *ACS App. Mat. Inter.*, 2017, **9**, 7115–

7124.

48. H. Wang, K. J. Yakal-Kremski, T. Yeh, G. M. Rupp, A. Limbeck, J. Fleig and S. A. Barnett, *J. Electrochem. Soc.*, 2016, **163**, F581–F585.

49. M. Niania, R. Podor, T. B. Britton, C. Li, S. J. Cooper, N. Svetkov, S. Skinner and J. Kilner, *J. Mater. Chem. A*, 2018, **6**, 14120–14135.

50. G. A. Hughes, K. Yakal-Kremski and S. A. Barnett, *Phy. Chem. Chem. Phy.*, 2013, **15**, 17257–17262.

51. M. S. Khan, X. Xu, J. Zhao, R. Knibbe and Z. Zhu, *J. Power Sources*, 2017, **359**, 104–110.

52. K.-Y. Lai and A. Manthiram, *J. Mater. Chem. A*, 2019, **7**, 8540–8549.

53. C. J. Gommes, A.-J. Bons, S. Blacher, J. H. Dunsmuir and A. H. Tsou, *Aiche J.*, 2009, **55**, 2000–2012.